Current State of Reduced Solar Activity: Intense Geomagnetic Storms

P.K. Manoharan [1], K. Mahalakshmi [1], A. Johri [1], B.V. Jackson [2], D. Ravikumar [1], K. Kalyanasundaram [1], S.P. Subramanian [1], A. K. Mittal [1]

[1] Radio Astronomy Centre, National Centre for Radio Astrophysics, Tata Institute of Fundamental Research, Udhagamandalam (Ooty), India.
[2] Center for Astrophysics and Space Sciences, University of California, San Diego, La Jolla, USA

E mail (mano@ncra.tifr.res.in).

Accepted : 22 October 2018

Abstract: We present a study of 21 geomagnetic storms, occurred during 2011–2017 in association with the propagation of coronal mass ejections (CMEs). These storms are selected with the minimum storm disturbance index (SYM-H) intensity of -100 nT or less and are distributed from the maximum to the minimum of the weak solar cycle 24. We identify and investigate these storm-driving CMEs (halo and partial halo CMEs) by combining EUV and white-light images in the near-Sun region, interplanetary scintillation images in between the Sun and the Earth, and in-situ measurements at the near-Earth orbit. These CMEs cover a wide range of initial speeds, ~180 to 2680 km/s. For about 50% of the CMEs, the fast initial speed at the near-Sun region does not correlate with the final speed at the near-Earth orbit. The storm indexes range between -100 and -233 nT and they are associated with minimum Bz values in the range of -12 to -38 nT. The Forbush decrease (FD) levels associated with these storms vary in the range of about -2% to -10%. A comparison of travel times of CMEs to 1 AU with the observed initial/final speeds and estimated initial speed suggests that a large fraction of fast initial speeds could possibly be due to the sudden expansion of the CME into a relatively low pressure interplanetary medium. Most of the geomagnetic storms (i.e., 19 storms) have been caused by the strong intrinsic magnetic field of the CME and only 2 storms are produced by the sheath region between the arrival times of interplanetary shock and CME. The geomagnetic storm index is compared with the possible reconnection electric field component, BzV_{ICME}. It suggests an empirical relationship for the likely lower level of storm index, SYM-H = -70 - 0.003·BzV_{ICME}. (nT), in which Bz and V_{ICME} are respectively given in units of nT and km/s.

Keywords: solar activity, coronal mass ejections, interplanetary shocks, interplanetary scintillation, geomagnetic storms, Space Weather, United Nations, COPUOS, IHY2007, ISWI,

Introduction

Solar Cycle 24 is the weakest cycle in a time period of more than a century. This cycle started to rise slowly from the unusually deep and significantly prolonged minimum activity of the previous cycle (e.g., Manoharan, 2012; Basu, 2016; Pesnell, 2016; Cliver and von Steiger, 2017). The weak polar field during the above minimum phase has led to the weak maximum, an asynchronous reversal of polar fields, and the hemispheric asymmetry in cycle 24. It has been shown by several observations that the overall magnetic field of the Sun has been low during the cycle 24 compared with previous cycles (e.g., Hathaway, 2015 and references therein). The consequences of the weak activity has also resulted in the lowest solar wind power output and a large decrease in the magnitude of the interplanetary magnetic field in the heliosphere (e.g., McComas et al., 2013; Gopalswamy et al., 2014). These effects in turn have affected the propagation of CMEs and formation of their associated shocks (Manoharan et al., 2016; Cliver and von Steiger, 2017). Concerning geomagnetic storms, the weak cycle has caused a smaller number of severe storms (Dst/SYM-H < -200 nT) and relatively less impact has been observed in near-Earth space (e.g., Richardson, 2013; Gopalswamy et al., 2015a,b; Lee et al., 2017). In solar cycles 23 and 24, respectively, the averages of moderate to intense geomagnetic storms intensities are comparable, but there is a large reduction of about 80% in number of intense storms during the cycle 24 (Selvakumaran et al., 2016; Watari, 2017; Scolini et al., 2018). Here we study these events, which have caused appreciable activity at the Earth's magnetosphere.

Intense Geomagnetic Storms of Cycle 24

In this study, we examine CME events responsible for 21 intense geomagnetic storms, which are considered based on a minimum threshold of storm disturbance index, SYM-H, of strength -100 nT or less. A geomagnetic storm with a SYM-H (or Dst) intensity close to or below this level in general is considered a major storm (e.g., Tsurutani and Gonzalez, 1997). It is to be noted that Dst and SYM-H are equivalent and SYM-H is useful to study geomagnetic storms with a higher temporal resolution. We here use the SYM-H index to measure the intensity of geomagnetic storms, which are listed in Table 1. In the current cycle, the strongest storm, SYM-H ≈ -233 nT, has been observed in association with the fast halo CME event on March 15, 2015 (Wu et al., 2016). However, the strength of this storm is relatively low in comparison with intense storms observed in the previous cycles. Moreover, some authors have also reported an overall low level of geomagnetic activity during the part of ascending phase of the cycle 24 (e.g., Richardson, 2013; Watari, 2017). The period of the present study covers between 2011 and 2017 in the descending phase of the cycle, which is more than half of the cycle, approximately from the beginning of the maximum phase to its minimum phase. In this period of study, some intense storms have also been driven by the interaction of high-speed wind from the coronal hole with low-speed wind and they are not analyzed/included. Table 1 lists 21 intense geomagnetic events examined in this study. It may be noted that excluding 3 X-class flare events, all other events are associated with moderate to less intense flares. Another interesting point is that 8 events correspond to insignificant flares and filament/prominence eruptions. The table includes each event's storm index, properties of its associated CME in the near-Sun region and its originating location on the solar disk, which gives an idea about the direction of propagation of the CME with respect to the Sun-Earth line. These CMEs were associated with shocks at 1 AU. The interplanetary shock (IP shock) and interplanetary CME (ICME) at 1 AU have been identified from in-situ measurements at the near-Earth orbit. The analysis procedure and discussion of propagation of a sample event from the Sun to Earth's orbit is described in the following sections.

Analysis of Propagation of a CME: Sun to near-Earth Space

For a given storm event, the source location of its corresponding CME on the solar disk has been identified using the images from Solar Dynamic Observatory (SDO) (Pesnell, Thompson, and Chamberlin, 2012) observed in the wavelength band of 193 Å. The initial speed and width of the CMEs near the Sun have been obtained from the white-light images of the LASCO coronagraphs (Brueckner et al., 1995) on board the SOHO spacecraft. In this study, we also use the LASCO-CME catalog and its supportive data generated and maintained at the CDAW Data Center (*https://cdaw.gsfc.nasa.gov/CME_list;* also refer to the studies presented about the CME catalog in Yashiro et al., 2004 and Gopalswamy et al., 2009). In Figure 1a, we display a sample image of an M2/1N flare obtained from the SDO in the wavelength band of 193 Å at 01:48 UT on 21 June 2015 (*https://cdaw.gsfc.nasa.gov/movie/make_javamovie.php?date=20150621&img1=sdo_a193&img2=lasc2rdf*). The flare occurred in the north-east part of the solar disk at N12E13. In association with this flare event, the onset of a full halo CME was observed at 02:36 UT in the LASCO C2 coronagraph. Figures 1b and 1c show the white-light images from the C2 and C3 LASCO coronagraphs, which cover a field of view of about 2–30 solar radii (*https://sohowww.nascom.nasa.gov/data*). The LASCO images reveal that the CME propagated fast at an average linear speed of ~1365 km/s, as measured in the north-eastern direction along a position angle range of ~50–70^{o}. Since the above speed estimation is in the plane of the sky, the speed may be likely affected by the projection effects.

The properties of the CME obtained from the LASCO images have been combined with the interplanetary scintillation (IPS) measurements, whenever available, from the Ooty Radio Telescope (ORT) to infer the typical propagation characteristics of the CME at an approximate heliocentric distance midway between the Sun and 1 AU (for details on ORT, refer to Swarup et al., 1971). Figure 2a displays an Ooty IPS image of the interplanetary medium on 22 June 2015. This IPS image has been made with normalized scintillation indexes, i.e., g-values, from a large number of radio sources on 22 June 2015, observed in the time range of ~05:30–15:00 UT (refer to Johri and Manoharan, 2016, for details about the IPS observation/analysis with the ORT). This raw IPS image is analogous to the LASCO white-light image, but covers a wider field of view extending over 90° with respect to the Sun. The fast expanding halo CME occurring on 21 June 2015 can evidently be seen as enhanced level of scintillation in the east as well as the west of the Sun. The ORT employed is capable of tracking a radio source for about 9.5 hours. However, for the IPS observations reported here, the telescope was parked at a desirable hour-angle position to record the passage or crossing of the CME and the scintillating sources transiting at the beam of the telescope were observed by simply switching the declination pointing toward the source. The above snapshot image has been made with the normalized scintillating levels of several such transited sources and the observing time on the scintillation image typically increases from the west of the Sun (i.e., right side of the image) to the east (i.e., left side of the image). That is, the sources located west of the Sun transit at the telescope earlier than those located east of the Sun.

Figure 2b shows the image of the ecliptic view of heliospheric density on 22 June 2015 at 18 UT, obtained from the tomography reconstruction of Ooty IPS measurements, which are selected when both g-value and velocity estimates are available for a given source. The reconstruction of the Ooty data is made typically for each solar rotation using the time-dependent computer-assisted tomography technique, developed by B.V. Jackson and his team (e.g., Jackson et al., 2003; Bisi et al., 2009). In the reconstructed image, the propagating CME can be seen as a large structure of high density close to the orbit of Earth. The central part is denser than its exterior parts. In comparison with the raw snapshot image (Figure 2a), which suffers the line of sight integration, the reconstruction provides a much clearer view of the propagating structures. When the onset of the CME in the LASCO field of view is compared with the appearance of the CME in the IPS field of view, it provides an approximate speed of about 800 to 850 km/s at a distance of ~0.5 AU and this speed is in good agreement with the IPS speed estimates made on individual radio sources, whose lines of sight pass through the propagating CME. The above speed is the bulk speed estimated from the appearance of the CME in the IPS field of view with respect to the LASCO field of view (e.g., Manoharan et al., 2001). Figure 2c includes also estimates of g-value and solar wind speed from IPS measurements on several sources as functions of observing time and heliocentric distance. In Figures 2a-c, the enhanced levels of scintillation/density and velocity show the propagating structures associated with the CME.

Every storm-driving CME's corresponding IP shock and ICME have been identified using in-situ magnetic field and solar wind plasma data sets, spanning over a period of about a day to 5 days after the onset of the CME. In this study, we use OMNI high-resolution interplanetary data sets available at *https://omniweb.gsfc.nasa.gov* (e.g., King and Papitashvili, 2005). The arrival times of IP shock and ICME have been useful to identify the corresponding geomagnetic storm recorded by the ground-based observatories. However, for some cases, the unique association of the CME with its corresponding IP shock (as well as ICME and geomagnetic storm) was difficult during the period of multiple CME/flare eruptions and/or during high-speed stream interactions, which resulted in a complex interplanetary medium.

In Figure 3, in-situ and ground-based measurements are plotted as a function of day number including data for the IP shock and ICME of the event occurred on 21 June 2015. The arrival times of the shock and ICME are indicated, respectively, by red and blue dashed-vertical lines. The sudden discontinuities in IP magnetic field and solar wind plasma data show the arrival of the shock. Whereas the identification of the ICME at 1 AU has been made with one or more of the following solar wind plasma and/or magnetic field characteristics, (a) strong average magnetic field, (b) smooth latitudinal rotation of the Bz component (in GSM coordinate system) (c) reduced level of proton temperature, (d) low value of plasma beta, and (e) counter-streaming of electrons (e.g., Manoharan et al., 2004). Figure 3 includes the stack plots of following parameters observed with a temporal resolution of 5-min during 22 - 23 June 2015: (i) average and Bz component of the IP magnetic field, (ii) speed, density, and temperature of the solar wind plasma, (iii) plasma beta (β) parameter, which is the ratio of plasma pressure to magnetic pressure, $(Nk_bT)/(B^2/2\mu_o)$, where N and T are the solar wind density and temperature, and B is the strength of the magnetic field, and (iv) geomagnetic storm intensity index, SYM-H (plus Dst index plotted with 1-hour resolution), (v) distribution of cosmic ray modulation (i.e., Forbush decreases, FD) as recorded by a network of neutron monitoring stations distributed over a large range of geographic latitudes as well as longitudes, and (vi) profile of proton flux detected by the near-Earth satellite in the energy range >10 MeV. The halo CME event on 21 June 2015 caused a fast IP shock (speed ~ 750 km/s) at 18:35 UT on 22 June, followed by the crossing of the ICME (speed ~710 km/s) at the early hours on 23 June. The above discussed IPS observations (Figure 2) as well as the spacecraft data sets are consistent with the arrival time of the ICME at the Earth's magnetosphere. The time periods before and after the interval discussed in Figure 3 have also shown to have a compound event with possibly more than one shock and ICME (e.g., Liu et al., 2015; Manoharan et al., 2016; Webb and Nitta, 2017).

As shown in Figure 3, in the time interval between the arrivals of the IP shock and ICME (i.e., in the compressed sheath region), the Bz component (measured in the GSM coordinate system) of

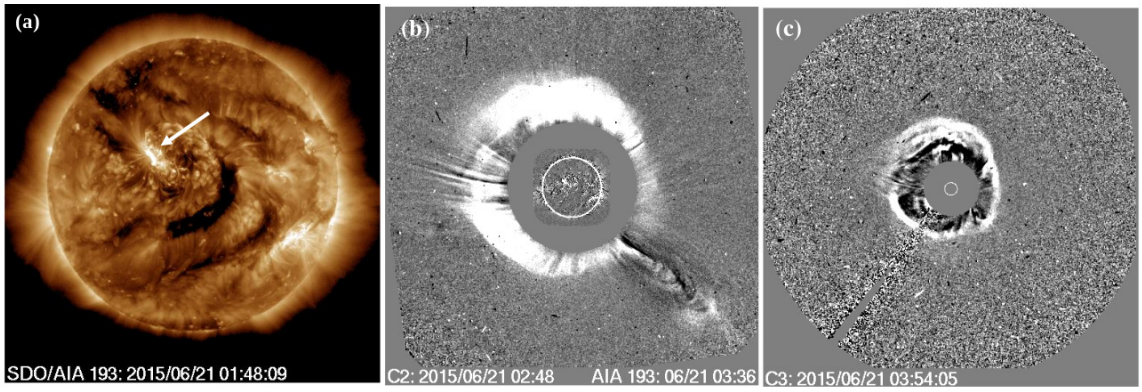

Figure 1: (a) An image from Solar Dynamic Observatory at 193 Å of an M2/1N flare at 01:48 UT on 21 June 2015 (*https://cdaw.gsfc.nasa.gov/movie/make_javamovie.php?date=20150621&img1=sdo_a193&img2=lasc2rdf*). The arrow mark indicates the flaring location on the Sun. (b and c) LASCO white-light running difference images, respectively, from C2 (at 02:48 UT) and C3 (at 03:54 UT) coronagraphs. In these images, the central circle represents the position of the solar disk. The propagation of the halo CME associated with the above flare can be seen clearly in these images.

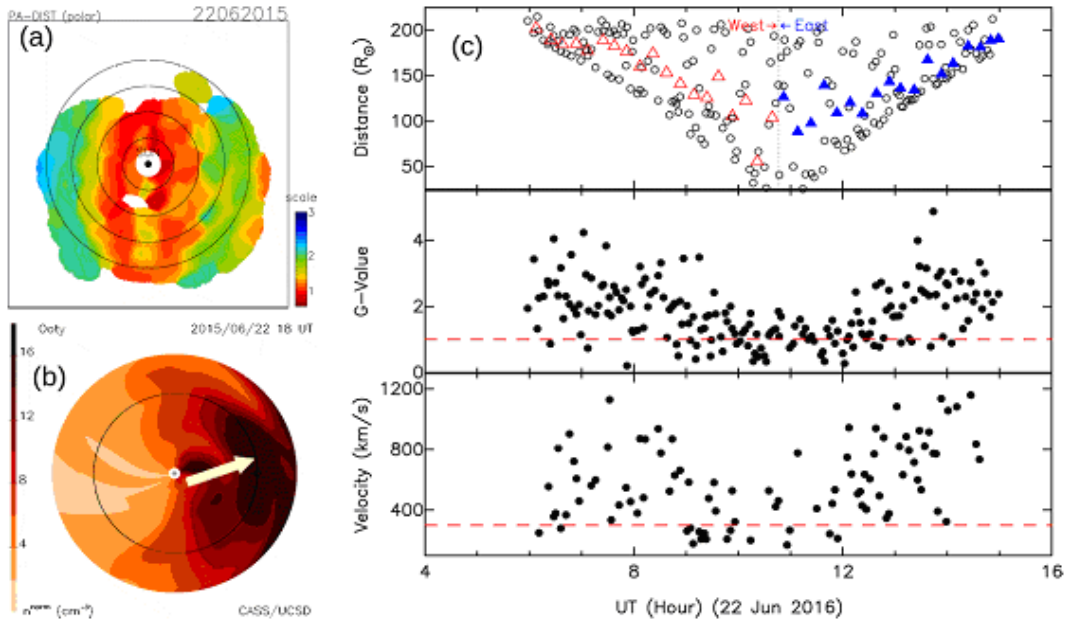

Figure 2: (a) The raw IPS snapshot image (based on g-values of several sources) observed with the Ooty Radio Telescope, during ~05:30-15:00 UT on 22 June 2015. It represents the snapshot sky-plane image (analogous to LASCO white-light image). The color code indicates the low-level of g-value (red color code) to high-level (blue color code). The concentric circles are at 50 solar radii interval. (b) The solar wind density image obtained from the 3-D tomographic reconstruction of the Ooty IPS measurements. In this an ecliptic plane view image, the circle represents the orbit of the Earth and the black dot on it shows the position of the Earth. The arrow shows the central part of the CME crossing the Earth. (c) Time series of IPS estimates (velocity and g-level) on 22 June 2015. Each dot on the plot corresponds to an IPS source. The top panel shows the distribution of closest approach heliocentric distances of observed sources (p = sin(ε) in solar radii, where ε is the solar elongation; i.e., p is the closest solar approach distance of the line of sight to the radio source). Each triangle symbol (i.e., red (west of Sun) and blue (east of Sun), respectively) represents average heliocentric distance over an observing time period of ~20 minutes. In the bottom and middle panels, the propagating CME structures can be evidently seen from the high speed data points (above the background speed of ~350 km/s and the typical background solar speed is indicated by dashed red line) and high g-level/density values (a g-level≈1 represents the background or ambient solar wind and it is shown by the dashed red line).

the IP magnetic field shows large oscillations and it drops for a short duration to a minimum value of -38 nT, in which situation the IP magnetic field is mostly pointed toward the southern direction. The negative value of Bz can be geoeffective. This value of Bz = -38 nT is the lowest value of Bz observed in all these storms. The sheath region has also been responsible for an intense geomagnetic storm of intensity -135 nT, at 20:15 UT on 22 June. However, a much more intense storm of strength -207 nT at 04:25 UT on 23 June has been recorded after the arrival of the ICME, in which the intrinsic magnetic cloud shows a relatively prolonged negative Bz component. Additionally, the above IP shock has been strong enough that in relation to it, a strong magnetic pulse of intensity +77 nT has also been recorded in the SYM-H index, suggesting the involvement of a severe dynamic pressure pulse of the solar wind at the Earth's magnetosphere. Further, an intense shock storm particle event has been observed immediately after the arrival of IP shock at a level of about 5 times above the background proton flux at energies >10 MeV. The cosmic ray flux also shows a minor positive peak near the time of the IP shock. While the passing of the ICME through the magnetosphere of the Earth, a considerable level of Forbush decrease (FD) has been recorded in the network of neutron monitors. However, the level of FD shows a large north-south geographic latitudinal asymmetry and the reduction of cosmic ray flux varies from about 3 to 8%.

Table 1: List of Geomagnetic Storms and their Associated Coronal Mass Ejections

	IP Shock Data				ICME Data			LASCO CME and Flare Data					SYM-H Index			Cloud/	V_{IPS}
No	Date	Time	V_{SH} km/s	M_a	M_s	Date	Time	V_{IC} km/s	Date	Time	V_{LAS} km/s	Flare class	Flare Loc	Date	Time	Index nT	sheath (C/S)	km/s
01	20110805	1745	880	10.8	7.1	20110805	2030	622	20110804	0412	1315	M9.3/2B	N19W36	20110806	0320	-126	C	–
02	20110926	1230	648	7.9	5.9	20110926	1650	584	20110924	1248	1915	M7.1	N10E56	20110926	2235	-111	C	–
03	20111024	1830	548	4.8	3.7	20111025	0110	502	20111022	1024	1005	M1.3	N25W77	20111025	0115	-160	C	–
04	20120308	1100	815	4.9	4.1	20120308	2020	652	20120307	0024	2684	X5.4/3B	N17E27	20120309	0755	-149	C	900
05	20120423	0320	423	3.6	2.4	20120423	1755	389	20120419	1512	540	flmt	S36E71	20120424	0325	-125	C	500
06	20120714	1805	671	5.2	4.5	20120715	0650	616	20120712	1648	885	X1.4	S15W01	20120715	1000	-122	C	750
07	20120930	2305	459	3.6	3.0	20121001	0200	407	20120928	0012	947	C3.7	N06W34	20121001	0355	-138	C	600
08	20121008	0520	450	2.1	1.9	20121008	1835	401	20121005	0248	612	B7.8	S23W31	20121009	0210	-116	C	500
09	20121112	2305	500	1.5	1.6	20121113	0855	423	20121109	1512	559		S26E34	20121114	0725	-117	C	550
10	20130317	0545	763	6.6	5.3	20130317	1040	713	20130315	0712	1063		N11E12	20130317	2025	-131	C	850
11	20130531	1620	453	3.8	3.4	20130601	0100	397	20130527	1924	530		SE	20130601	0745	-134	C/S	–
12	20130627	1440	482	2.5	2.2	20130628	0225	410	20130624	0400	709		S26W65	20130629	0630	-110	C	550
13	20140219	0345	544	1.2	1.2	20140219	1400	516	20140216	1000	634	M1.1/SN	S11E01	20140219	0820	-125	S	650
14	20140227	1650	510	3.9	3.4	20140228	0255	470	20140225	0126	2147	X4.9/2B	S12E82	20140227	2325	-100	S	–
15	20150317	0440	630	4.3	3.9	20150317	1355	591	20150315	0148	719	C9.1/1F	S22W25	20150317	2245	-233	C	800
16	20150622	1835	765	5.5	4.0	20150623	0050	710	20150621	0236	1366	M2.0/1N	N12E13	20150623	0425	-207	C	850
17	20151219	1615	500	3.0	2.6	20151220	0050	455	20151216	0936	579	C6.6/1F	S13W04	20151220	2250	-169	C	550
18	20151231	0100	470	2.4	2.2	20151231	1910	452	20151228	1212	1212	M1.8	S20W20	20160101	0105	-117	C	600
19	20161012	2210	435	3.0	2.6	20161013	0605	420	20161009	0224	179			20161013	2345	-114	C	450
20	20170527	1540	390	3.8	3.0	20170527	2145	368	20170523	0500	259	flmt	S07E01	20170528	0710	-141	C	400
21	20170907	2310	1019	3.7	3.7	20170908	1140	784	20170906	1224	1567	X9.3	S08W33	20170908	0105	-144	C	1000

Date and Time are, respectively, given in formats *yyyymmdd* and *hhmm*

V_{SH} = IP shock speed at 1 AU; M_a = Alfvenic Mach number; M_s = Magnetosonic Mach number

V_{IC} = ICME speed at 1 AU; V_{LAS} = near-Sun LASCO speed; V_{IPS} = CME speed at ~0.5 AU from IPS measurements

ICME/sheath: C – ICME/Magnetic cloud caused the main storm; S – Sheath caused the main storm

Results and Discussion

The above analysis procedure has been followed for all 21 intense storm events. A careful examination as well as comparison of the IP magnetic field data and geomagnetic storm index reveals that the Bz component of the IP magnetic field is well correlated with the strength of geomagnetic index. In these, 19 geomagnetic storms have mainly been associated with the negative Bz component of the ICME and/or magnetic cloud and 2 storms have been produced by the magnetic field in the compression or sheath region, between the arrivals of shock and ICME. Each FD associated with these geomagnetic storms show different levels, from a decrease of about -2% up to about -10%. It is to be noted that in these CMEs, only 12 of them are Earth-directed events (originating locations within ±35 deg. from the center of the solar disk). However, since all of them are fast and wide (halo and partial halo CMEs of width >160 deg.) as well as due to the propagation effects such as deflection and/or rotation, the portion of the CME or its corresponding shocked solar wind structure grazing/passing the magnetosphere of the Earth could cause the intense storm. When we examine the initial speed of individual CMEs in the LASCO field of view, 19 of them traveled well above the ambient solar wind speed and 2 events started although with low initial speeds, but attained speeds faster than the background wind at the end of the LASCO field of view. The average speed of these CMEs is $<V_{LASCO}>$ ~990 km/s; but, the individual initial speeds show a large range from ~180 to 2680 km/s. (It should be noted that the initial speed of a CME measured by the LASCO is the speed projected on the sky-plane and the underestimation caused by the projection varies depending on the originating location of the CME on the solar disk (e.g., Manoharan, 2006)). Moreover, as indicated by the available IPS data, these CMEs traveled considerably fast, $<V_{IPS}>$ ~ 750 km/s, at a distance of about 0.5 AU in the inner heliosphere. These CMEs were also associated with strong IP shocks at 1AU: average magnetosonic Mach number is <Ms> = 3.4; the average Alfvenic Mach number is <Ma> = 4.2; the average shock speed is $<V_{SHOCK}>$ = 590 km/s. Some of the shocks have been strong enough to produce a significant amount of flux of storm particles.

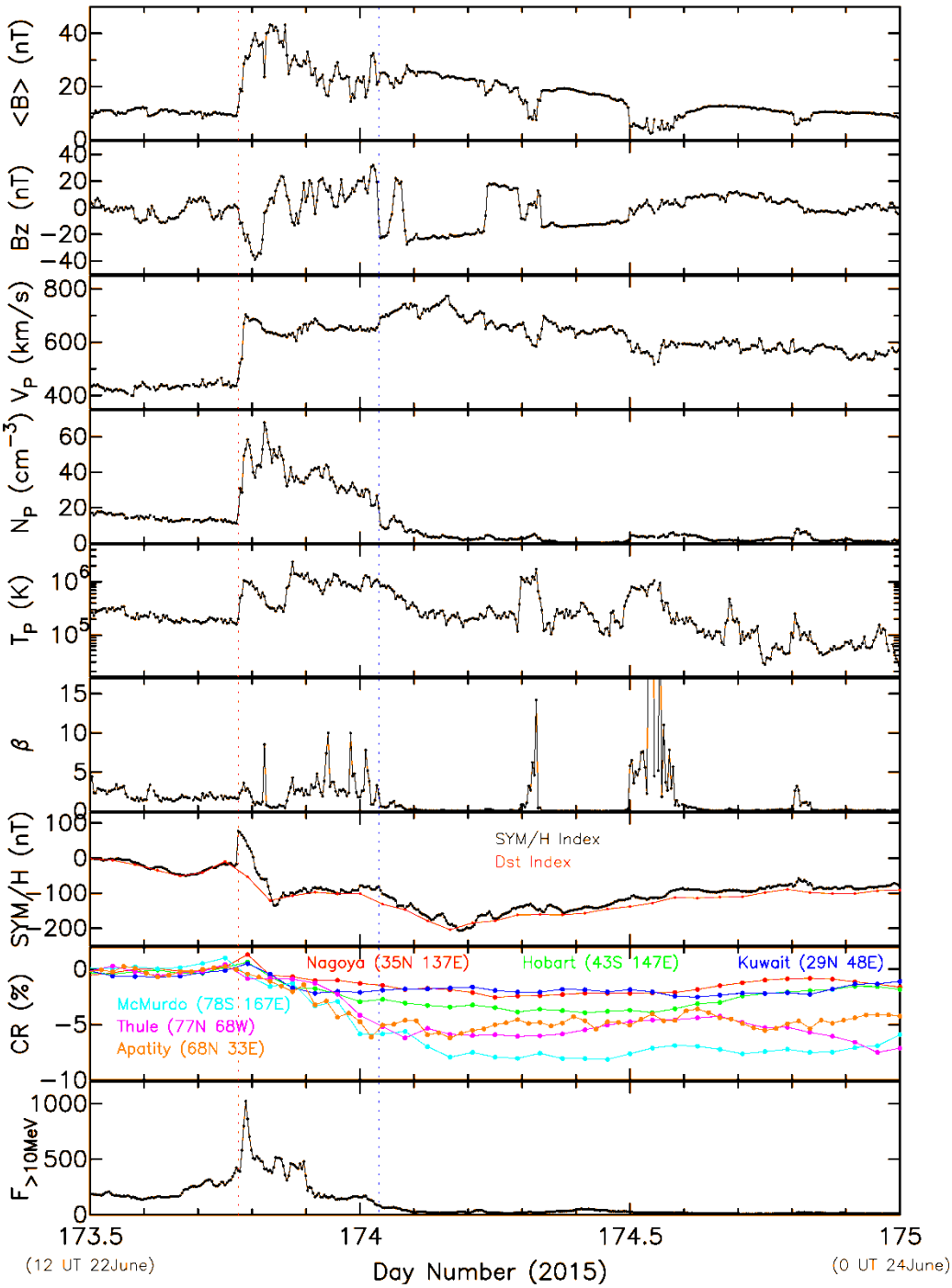

Figure 3: Stack plots of IP magnetic field (<B> and Bz (in GSM coordinate system)) measurements and solar wind parameters (proton speed (Vp), density (Np), temperature (Tp), and plasma beta (ß)), during day numbers 173.5 – 175 (22 and 23 June 2015). This figure also includes SYM-H and Dst indexes, percentage decrease of cosmic ray flux (CR) recorded by several neutron monitoring stations, and proton flux at energies >10 MeV. All the data sets are at 5-min resolution (obtained from OMNI data available at https://omniweb.gsfc.nasa.gov), except Dst index and FD data, which are at hourly resolution.

For the present list of major storm events (Table 1), in-situ solar wind parameters and IP magnetic field data have been carefully examined and compared with the list of common 12 intense storms reviewed by Gopalswamy et at. (2015a). Since the study by Gopalswamy et al. (2015a) has considered the Dst index based on one-hour resolution data, their indexes are marginally lower than the SYM-H indexes reported in the present analysis and on the whole the results of their events are consistent with the present study. Some of the detailed findings are: (1) In the case of CME event on 04 August 2011 (refer to Table1, event #1), it would have likely interacted with the previous slow halo CME originated nearly at the same location about 10 hours earlier. In the in-situ data, we could also identify two IP shocks, respectively, at 17:45 UT and 19:00 UT on 05 August. However, the magnetic storm seems to peak after the arrival of the ICME (also interaction between CMEs has likely led to a complex structure). (2) Similarly, the storms associated with the second and third CME events have been considered after the arrival of their respective ICMEs. (3) For CME events on 28 September 2012 (event #7) and 15 March 2013 (event #10), the storms start to develop during the period of the sheath and however they peak (attain lowest SYM-H values) after the arrival of the respective ICMEs. Thus, the storm events peaked after the arrival of the ICME have been considered to be associated with their respective ICMEs. (4) The analysis of event #11 on 27 May 2013 was rather difficult and Gopalswamy et al. (2015a) reported its association with a stream interaction

region. The identification of the CME in the near-Sun region was an involved process and the CME recorded by the LASCO showed association with a back-side CME as observed by STEREO A and B space missions. STEREO-B observed the event at the west side of the central meridian of the Sun and STEREO-A saw it as a CME just behind the west limb of the Sun (refer to https://stereo-ssc.nascom.nasa.gov) and with respect to LASCO, it would be in the south-east direction. But, the CME speed estimated from the STEREO-A was less than of the LASCO speed. If the same event was recorded as a limb event by STEREO-A, the projection effect should be minimum and its speed should be the highest. It is possible that two CMEs occurred nearly at the same time. In the in-situ data sets, 2 IP shocks were observed, separated by ~20 hours, possibly the first one was associated with the CME and the second was due to the stream interaction region. The arrival of the first shock at 16:20 UT on 31 May 2013 was followed by the typical ICME signatures (electron fluxes were also examined). Moreover, nearly at the time of arrival of the second shock at about 07:40 UT on 01 June 2013, the storm maximized at -134 nT. The high-speed stream followed after the arrival of the second shock. Also by examining the speeds of these shocks, we consider the storm to be associated with the arrival of the CME event.

For nearly all events considered in this study, at the time of minimum Bz, the other components (i.e., Bx and By) were less than the Bz value, suggesting the storm has been dominated by the southward orientation of the magnetic field. The average speed of the ICMEs at 1 AU is $<V_{ICME}>$ = 520 km/s and the spread in ICME speeds is considerably smaller compared to the range observed in the initial speeds at the LASCO field of view (refer to Table 1). This result although is consistent with the previous studies (e.g., Gopalswamy et al., 2000; Manoharan et al., 2004; Manoharan 2006; Manoharan and Rahman, 2011), the present 1-AU average speed is higher than that of the previous cycle. Therefore, the initial speed, the transit time, and the average transit speed of each CME are further examined. The time difference between the onset of the CME at the LASCO field of view and the arrival of the ICME at 1 AU provides its transit time. Depending on the speed of the propagation, transit times range between ~40 to 110 hours. In Figure 4 (*right plot*), we compare the transit time with the initial speed at the LASCO field of view and it shows a large scatter in travel time for a given CME speed. On the other hand, as illustrated in Figure 4 (*left plot*), the travel time shows a systematic increase with the decreasing ICME speed at 1 AU (shown as red dots). However, the plot is for the final

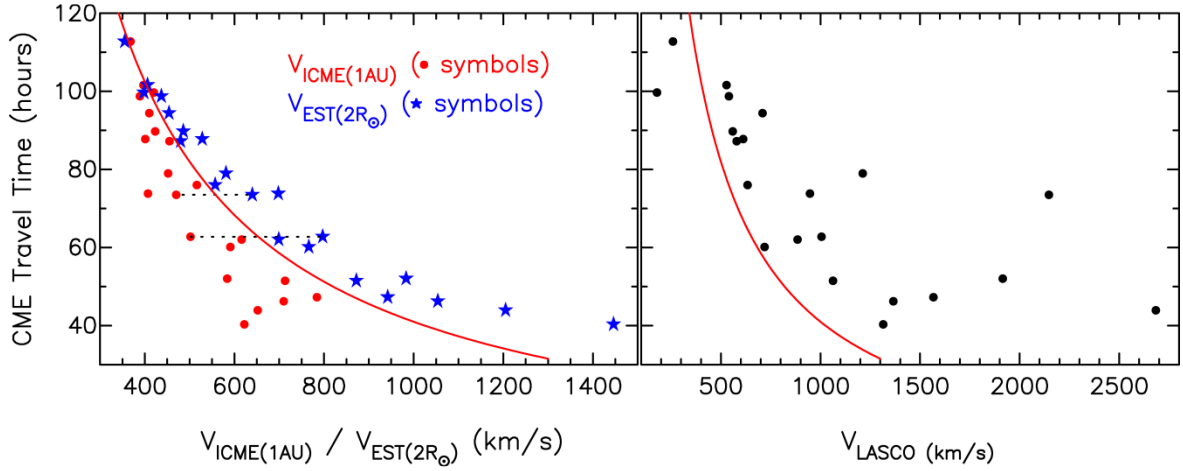

Figure 4: (*left*) The transit time of the CME from the LASCO field of view to the orbit of the Earth is plotted against the observed in-situ speed of the ICME at 1 AU (red dot symbols). The red curve shows the computed travel time using the ICME speed at 1 AU, with the assumption that the CME traveled at a constant speed, V_{ICME}, from Sun to Earth. The observed travel time and final speed at 1 AU are employed to estimate the average speed of the CME as well the possible speed, V_{EST}, at the LASCO field of view (refer to equation 1). The estimated initial speeds (V_{EST}) are plotted as blue star symbols. (*right*) The transit time of the CME plotted as function of initial speed of the CME, V_{LASCO}. The red curve is shown as a reference, which is same as the above plot. Except for two CMEs located at the left of continuous curve, all the events decelerated in the Sun-Earth distance.

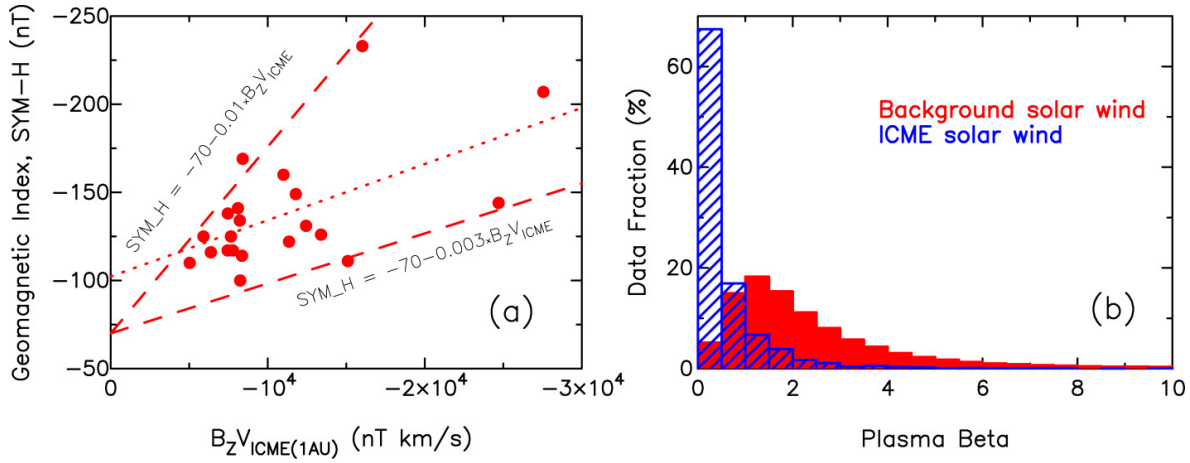

Figure 5: (a) Geomagnetic index, SYM-H, plotted as a function of product of southward component of interplanetary magnetic field and in-situ speed of ICME at 1 AU (i.e., B_zV_{ICME}). The dotted line is the best fit to the data points . The two dashed lines indicate, respectively, upper and lower boundaries of the geomagnetic index for a given value of B_zV_{ICME}. (b) Distributions of 5-min data points of plasma beta during the period 2011 – 2017. The histogram shown in red represents the ambient solar wind, V < 400 km/s, condition. The histogram shown in blue corresponds to ICMEs plasma data, covering a day-long period starting at the onset of each ICME at 1 AU.

speed of the CME. A large range of initial speeds in the near-Sun region and the systematic behavior seen in Figure 4 indicate that CMEs have likely gone through considerable evolution. Since the travel time and V_{ICME} are observed quantities, they are useful to infer the initial conditions of the CME in the LASCO field of view. For example, the transit time and the average transit speed (V_{AVG}) (e.g., Manoharan and Rahman, 2011) are useful to understand the overall evolution of the CME,

$$V_{AVG} = \frac{1AU}{CMETransitTime} = \frac{V_{EST} + V_{ICME}}{2} \quad (1)$$

Thus the observed transit time and speed of the V_{ICME} at 1 AU can be used to estimate the typical starting speed, V_{EST}, of the CME at the onset distance of the LASCO coronagraph, i.e., at ~2 solar radii, assuming that the CME has gone through a linear deceleration or acceleration. The estimated initial speed (V_{EST}) and the ICME speed at 1 AU (V_{ICM}) are useful to understand the speed evolution of a CME in the Sun-Earth distance and it may not be however helpful in predicting the arrival of the CME at 1 AU. It is seen that for about 50% of the events, the estimated initial speed, V_{EST}, has been much lower than the corresponding V_{LASCO}, suggesting that in these cases, the initial speed in the near-Sun region has probably been related to a sudden expansion of the CME. For example, Gopalswamy et al. (2014) also reported the anomalous expansion of CMEs observed in Cycle 24. As the CME propagated away from the LASCO field view, its speed has likely stabilized due to the equilibrium attained by the CME with the surrounding solar wind. It is to be noted that the LASCO speeds are measured in the plane of the sky and the actual CME initial speeds could have been higher than those recorded by the LASCO. In the present cases, even without taking the projection into account, the near-Sun LASCO speeds are largely higher than the estimated initial speeds, V_{EST}, and the consideration of projection may lead to larger deviations. The V_{EST} values are plotted as blue star symbols on Figure 4 against their corresponding transit times. The V_{ICME} and its corresponding V_{EST} are joined by dotted lines for 2 events and the width (i.e., $V_{EST} - V_{ICME}$) provides the effective acceleration experienced by the CME. It is interesting to note the increase in separation between V_{EST} and V_{ICME} as the travel time decreases or for increase of speed. For 19 events, V_{EST} is higher than its V_{ICME} and its shows the effective deceleration experienced by the CME in the solar wind. However, in the low-speed portion of the plot, 2 events show $V_{ICME} > V_{EST}$, suggesting that these events have gone through a marginal acceleration. In Figure 4, the red curve shows the transit time to 1 AU for a CME propagating at a constant speed equal to its final speed at 1 AU, i.e., V_{ICME}. This represents the average speed of propagation, V_{AVG} and the speed estimates obtained from IPS measurements at about 0.5 AU are consistent with the V_{AVG} estimates. For a given V_{ICME}, the above curve however gives a lesser travel time than that of the previous cycle (e.g., Manoharan and Rahman, 2011).

The storm indexes range between -100 to -233 nT (2 events are severe and their SYM-H values are less than -200 nT) and show an average of about -135 nT. The study includes more than half of the cycle from 2011 to 2017, i.e., from the maximum of the cycle to its minimum phase. However, the number of intense storms observed is less compared to the previous cycle. They do not show any preferential correlation with the initial speed of the CME. For all these storms, the minimum Bz values range between -38 and -12 nT, with an average of about -20.5 nT. However, the lowest value of Bz = -38 nT has been associated with the sheath region caused by the CME event on 21 June 2015 and this lowest value has been associated with a considerably lesser intense storm (SYM-H = -135 nT) than that produced by the ICME (SYM-H = -207 nT) (refer to Figure 3). Thus, a geomagnetic storm can mainly be caused by the southward magnetic field component of the ICME and/or of the sheath region between the shock and the ICME. The CME speed at the near-Earth space also plays an appreciable role in the production of a storm. Therefore, the correlation of the geomagnetic storm index, respectively, with Bz and with the convective component of the electric field, BzV_{ICME} has been the focus of several studies (e.g., Tsurutani and Gonzalez, 1997; Zhang et al., 2007; Gopalswamy, 2010). Figure 5(a) shows the scatter plot of geomagnetic index versus BzV_{ICME}. In this plot, the best-fit dotted line gives an empirical relation, SYM-H = -100 – 0.003 BzV_{ICME} (nT) (where Bz and V_{ICME} are, respectively, in units of km/s and nT) and it is nearly parallel to the possible lower boundary storm index, SYM-H = -70 – 0.003 BzV_{ICME} (nT), which is indicated as a dashed line. However, the observed scatter suggests that a steep upper boundary of the storm index, SYM-H = -70 – 0.01 BzV_{ICME} (nT). These equations provide a typical range of geomagnetic storms for minimum southward components and ICME speeds. For example in the upper index side, an ICME speed of ~1000 km/s and Bz = -50 nT would provide a storm index of -570 nT; whereas in the lower side, a typical speed of ~450 km/s and Bz = -20 nT would provide an index of ~ -100 nT. However, the range of storm indexes obtained from the above equation is marginally lower than the indexes derived for the previous cycle storms, Dst = -32 – 0.01BzV, as shown by Gopalswamy (2010).

In the present situation of weak solar activity (i.e., the power of the ambient solar wind is low), a magnetic cloud injected with a stronger intrinsic magnetic field than that of the ambient flow would quickly expand in course of its propagation and the field strength would also decrease (e.g., Gopalswamy et al., 2014). The other fact is that the compression and rotation of magnetic cloud could be an efficient mechanism, which would also lead to a high-level of geomagnetic storm (e.g., Webb et al., 2000). Since the background solar wind is largely prevailed by the low-speed flow, the above compression can be possibly ineffective.

Background Solar Wind Conditions

The above analysis indicates that for about 50% of the events, the initial speed is not consistent with the propagation time and/or final speed and these CMEs might have gone through sudden expansion, which possibly provides a high initial speed for short duration in the near-Sun region. However, the average speed of ICMEs at 1 AU is $\langle V_{ICME} \rangle$ = 520 km/s and most of the ICMEs show speeds well above the ambient speed. These facts suggest that the effect of deceleration imposed (i.e., drag force effected on the CME) by the low-speed dominated heliosphere on the propagation of CME has likely been overcome by the magnetic field associated with propagating CME. In order to understand the energy densities of the background solar wind and ICMEs, we study the distribution of plasma beta, β, of our in-situ data at 5-min resolution during the period of the study.

Figure 5(b) illustrates the typical histogram of the beta values at 1AU for solar wind speeds less than 400 km/s (i.e., typical ambient solar wind condition shown in red color). There is a clear peak around $\beta \approx 1.5$. The tail of the distribution extends to high values of β and nearly 80% of the data samples are distributed at values greater than 1. It may be noted that a value of beta, $\beta \approx 1.0$, corresponds to the equipartition of thermal and magnetic energy densities (or pressures). Moreover, a value of beta larger than the unity suggests an excessive thermal speed than that of the Alfven speed in the solar wind. Along with the above distribution, we also plot beta values of ICMEs investigated in the present study. For every ICME, one-day period is considered starting from the arrival of the ICME at the spacecraft (in Figure 3, ICME arrival time is shown by the blue vertical-dashed line). The distribution is consistent with the influence of magnetic energy density of ICMEs (i.e., magnetic clouds) and more than 85% of the data points fall below unity beta value. We have also reviewed distributions of density and temperature at 1 AU, respectively, for the ambient wind and ICME plasma. In these cases, unlike β distribution, about 60% of overlap is seen between the ambient and ICME plasma distributions. Taking into account of radial variations of temperature, density and magnetic field, the beta

distribution at 1 AU reveals that the magnetic energy has probably influenced the propagation of these storm-driving CMEs. When we examine, the distribution of β for intense storm events of the previous cycle, it is noticed that the β values are not as skewed towards the low value side. In the present storms, as far as the in-situ data are considered, the ICME plasma at 1 AU has been dominated by the magnetic pressure over the thermal pressure (energy densities are not in equipartition) and storms have been likely caused by the magnetic cloud configuration.

Summary:

Solar Cycle 24 is the weakest cycle since 1900. In this study, we have investigated the propagation characteristics of coronal mass ejections related to 21 intense geomagnetic storms during 2011 – 2017. This period covers the second half of the cycle 24, from the maximum phase to minimum phase. The storm indexes range between -100 and -233 nT and the minimum Bz values associated with them range between -12 and -38 nT. Out of these storms, 19 of them have been caused by the southward Bz component embedded in their corresponding CMEs and 2 storms have been produced by the sheath region between the arrivals of the IP shock and ICME. The observed storm strength and their related Bz values indicate that the cycle 24 is less geoeffective. Similar results have also been obtained for the first half of cycle 24 (e.g., Richardson, 2013; Gopalswamy et al., 2015b; Watari, 2017).

The CMEs associated with these intense storms show average speeds of 990 km/s and 520 km/s, respectively, in the near-Sun region and at 1 AU. A comparison of the initial and final speeds of fast CMEs (about 50% of the events) shows that the low-pressure of the solar wind has possibly caused the sudden expansion, resulting in a high speed propagation for a short distance from the Sun and these CMEs show no correlation with the final speed and transit time of the CME at 1 AU. An examination of the thermal and magnetic pressures of the ambient solar wind with that of storm producing interplanetary CMEs shows that the propagation is influenced by the magnetic energy of the CME. A comparison of geomagnetic storm indexes with the possible reconnection electric field component, BzV_{ICME}, suggests an empirical relationship for the upper level of storm index, SYM-H = -70 – $0.01 \cdot BzV_{ICME}$ (nT) and the results are consistent with the previous study by Gopalswamy et al. (2015b).

Acknowledgments

Part of this work was presented at the United Nations/United States of America Workshop on the International Space Weather Initiative: *The Decade after the International Heliophysical Year 2007* and PKM acknowledges the support provided to participate in the workshop. The authors thank the observing and engineering staff of the Radio Astronomy Centre (RAC) for help in making the IPS observations. The RAC is run by the National Centre for Radio Astrophysics of the Tata Institute of Fundamental Research. We thank the referees and their comments considerably improved the paper. The LASCO images are from the SOHO mission, which is a project of international cooperation between ESA and NASA. The authors would like to thank for the LASCO-CME catalog generated and maintained at the CDAW Data Center by NASA and the Catholic University of America in cooperation with the Naval Research Laboratory (https://cdaw.gsfc.nasa.gov/CME_list/). The authors thank Solar Dynamics Observatory (SDO) science teams for providing the high-resolution EUV images. The authors are grateful to the staff of Space Physics Data Facility, NASA/Goddard Space Flight Centre, who prepared and made available the OMNI data sets at *https://omniweb.gsfc.nasa.gov* and to Kyoto Geomagnetic Observatory for the SYM-H/Dst data sets. We acknowledge teams providing ground level cosmic ray monitoring data at http://cr0.izmiran.rssi.ru, NMDB database (www.nmdb.eu), and the Spaceship Earth network of neutron monitors (http://neutronm.bartol.udel.edu). The STEREO/SECCHI/COR2 CME catalog is generated and maintained at JHUAPL, in collaboration with the NRL and GSFC, and is supported by NASA.

References:

Basu, S.: 2016, Living Reviews in Solar Physics 13(2), doi: 10.1007/s41116-016-0003-4.

Bisi, M.M., Jackson, B.V., Clover, J.M., Manoharan, P.K., Tokumaru, M., Hick, P.P., and Buffington, A.: 2009, Ann. Geophys. 27, 4479–4489, doi: 10.5194/angeo-27-4479-2009.

Brueckner, G.E., Howard, R.A., Koomen, M.J., Korendyke, C.M., Michels, D.J., Moses, J.D., et al.: 1995, Solar Physics 162, 357, dio: 10.1007/BF00733434.

Cliver, E.W. and von Steiger, R.: 2017, Space Sci. Rev. 210, 227, doi: 10.1007/s11214-015-0224-1.

Gopalswamy, N., Lara, A., Lepping, R.P., Kaiser, M.L., Berdichevsky, D., St. Cyr, O.C.: 2000, Geophys. Res. Lett. 27(2), 145-148, doi: 10.1029/1999GL003639.

Gopalswamy, N., Yashiro, S. and Michalek, G. et al.: 2009, Earth Moon Planet 104, 295, doi: 10.1007/s11038-008-9282-7.

Gopalswamy, N.: 2010, in Proceedings of the IAU Symposium, vol. 264, edited by A. G. Kosovichev, A. H. Andrei, and J.-P. Rozelot, pp. 326–335, Cambridge Univ. Press, Cambridge, U.K, doi: 10.1017/S1743921309992870.

Gopalswamy N., Akiyama, S., Yashiro, S., Xie, H., Mäkelä, P., and Michalek. G.: 2014, Geophys. Res. Lett. 41, 2673–2680, doi: 10.1002/2014GL059858.

Gopalswamy, N., Tsurutani, B., and Yan, Y.: 2015a, Progress in Earth and Planetary Science 2, 13, doi: 10.1186/s40645-015-0043-8

Gopalswamy, N., Yashiro, S., Xie, H., Akiyama, S., Mäkelä, P.: 2015b, J. Geophys. Res. 120, 9221-9245, doi: 10.1002/2015JA021446.

Hathaway, D.H.: 2015, Living Reviews in Solar Physics 12(4), doi: 10.1007/lrsp-2015-4.

Jackson, B.V., Hick, P.P., Buffington, A., Kojima, M., Tokumaru, M., Fujiki, K., Ohmi, T., and Yamashita, M.: 2003, in M. Velli, et al. (eds.), American Institute of Physics Conference Series, 679, 75–78, doi: 10.1063/1.1618545.

Johri, A. and Manoharan, P.K.: 2016, Solar Physics 291, 1433-1446, doi: 10.1007/s11207-016-0900-7.

King, J.H. and Papitashvili, N.E.: 2005, J. Geophys. Res. 110, A02209, doi: 10.1029/2004JA010804.

Lee, C.O., Hara, T., Halekas, J.S., Thiemann, E., Chamberlin, P., Eparvier, F., Lillis, R.J., Larson, D.E., Dunn, P.A., Espley, J.R., Gruesbeck, J., Curry, S.M., Luhmann, J.G., and Jakosky, B.M.: 2017, J. Geophys. Res. 122, 2768-2794, doi: 10.1002/2016JA023495.

Liu, Y., Hu, H., Wang, R., Yang, Z., Zhu, B., Liu, Y.A., Luhmann, J.G., and Richardson, J.D.: 2015, Astrophys. J. Lett. 809, L34, doi: 10.1002/2017JA025131.

Manoharan, P.K., Tokumaru, M., Pick, M., Subramanian, P., Ipavich, F.M., Schenk, K., Kaiser, M.L., Lepping, R.P., Vourlidas, A.: 2001, The Astrophysical Journal 559, 1180–1189, doi: 10.1086/322332.

Manoharan, P.K., Gopalswamy, N., Yashiro, S., Lara, A., Michalek, G., and Howard, R.A.: 2004, J. Geophys. Res. 109, 6109, doi: 10.1029/2003JA010300.

Manoharan, P.K.: 2006, Solar Physics 235, 345, doi: 10.1007/s11207-006-0100-y.

Manoharan, P.K. and Rahman, A.M.: 2011, J. Atmos. Solar-Terr. Phys. 73, 671-677, doi:10.1016/j.jastp.2011.01.017.

Manoharan, P.K.: 2012, The Astrophysical Journal 751, 128, doi: 10.1088/0004-637X/751/2/128.

Manoharan, P.K., Maia, D., Johri, A., and Induja, M.S.: 2016, in: I. Dorotovic, C.E. Fischer and M. Temmer (eds.), Ground-based Solar Observations in the Space Instrumentation Era, Astronomical Society of the Pacific Conference Series, vol 504, pp. 59–66.

McComas, D.J., Angold, N., Elliott, H.A., Livadiotis, G., Schwadron, N.A., Skoug, R.M. and Smith, C.W.: 2013, The Astrophysical Journal 779, 2, doi: 10.1088/0004-637X/779/1/2.

Pesnell, W.D., Thompson, B.J., and Chamberlin, P.C.: 2012, Solar Phys. 275, 3, doi: 10.1007/s11207-011-9841-3.

Pesnell, W. D.: 2016, Space Weather 14, p. 10–21, doi: 10.1002/2015SW001304, 2016.

Richardson, I.G.: 2013, J. Space Weather Space Clim. 3, A08, doi: 10.1051/swsc/2013031.

Scolini, C., Messerotti, M., Poedts, S., and Rodriguez, L.: 2018, J. Space Weather Space Clim. 8, A09, doi: 10.1051/swsc/2017046.

Selvakumaran, R., Veenadhari, B., Akiyama, S., Pandya, M., Gopalswamy, N., Yashiro, S., Sandeep Kumar, Mäkelä, P., Xie, H.: 2016, J. Geophys. Res., 121, p. 8188–8202, doi: 10.1002/2016JA022885.

Swarup, G., Sarma, N., Joshi, M. et al.: 1971, Nature Physical Science 230, 185, doi: 10.1038/physci230185a0.

Tsurutani, B.T. and Gonzalez, W.D.: 1997, in B.T. Tsurutani et al. (eds), Magnetic Storms, Amer. Geophys. Union Press, Washington D.C., Mon. Ser. 98, p. 77, doi:10.1029/GM098p0077.

Watari, S.: 2017, Earth, Planets and Space 69, 70, doi: 10.1186/s40623-017-0653-z.

Webb, D.F., Lepping, R.P., Burlaga, L.F., DeForest, C.E., Larson, D.E., Martin, S.F., Plunkett, S.P., and Rust, D.M.: 2000, J. Geophys. Res. 105(A12), 27251–27259, doi: 10.1029/2000JA000021.

Webb, D. and Nitta, N.: 2017, Solar Physics 292, 142, doi: 10.1007/s11207-017-1166-4.

Wu, C-C., Liou, K., Lepping, R.P., Hutting, L., Plunkett, S., Howard, R.A. and Socker, D.: 2016, Earth, Planets and Space 68, 151, doi: 10.1186/s40623-016-0525-y.

Yashiro, S., Gopalswamy, N., Michalek, G., St. Cyr, O.C, Plunkett, S.P., Rich, N.B. and Howard, R.A.: 2004, J. Geophys. Res. 109, A07105, doi: 10.1029/2003JA010282.

Zhang, J., Richardson, I.G., Webb, D.F., Gopalswamy, N., et al.: 2007, J. Geophys. Res. 112, A10102, doi:10.1029/2007JA012321.